

~~Climatology, seasonality, and trends~~ A near-global climatology of oceanic coherent eddies

Josué Martínez-Moreno¹, Andrew McC. Hogg¹, and Matthew H. England²

¹Research School of Earth Science and ARC Center of Excellence for Climate Extremes, Australian National University, Canberra, Australia

²Climate Change Research Centre (CCRC), UNSW Australia, Sydney NSW, Australia

Key Points:

- Kinetic energy of coherent Coherent eddies contain around 50% of the surface ocean kinetic energy budget.
- Seasonal cycle of the number of coherent eddies and coherent eddy amplitude reveal a 3-6 month lag to wind forcing.
- Inverse cascade sets up the seasonal lag of The seasonal lag between the number and the amplitude of coherent eddies suggests a role for the inverse cascade.

14 **Abstract**

15 Ocean eddies influence regional and global climate through mixing and transport
 16 of heat and properties. One of the most recognizable and ubiquitous feature of oceanic
 17 eddies are coherent vortices with spatial scales of tens to hundreds of kilometers, frequently
 18 referred as “mesoscale eddies” ~~or “coherent eddies”~~. Coherent ~~Coherent mesoscale~~ ed-
 19 dies are known to transport properties across the ocean and to locally affect near-surface
 20 wind, cloud properties and rainfall patterns. Although coherent eddies are ubiquitous,
 21 ~~yet~~ their climatology, seasonality and long-term temporal evolution remains poorly un-
 22 derstood. ~~Thus~~Here, we examine the kinetic energy contained by coherent eddies and
 23 ~~we present the annual~~ present the seasonal, inter-annual and long-term ~~changes~~ variability
 24 of automatically identified coherent eddies from satellite observations from 1993 to 2019.
 25 Around 50% of the kinetic energy contained by ocean eddies corresponds to coherent ed-
 26 dies. Additionally, a strong ~~hemispherical~~ seasonal cycle is observed, with a 3–6 months
 27 lag between the wind forcing and the response of the coherent eddy field. ~~Furthermore,~~
 28 ~~the~~The seasonality of the number of coherent eddies and their amplitude reveals that
 29 the number of coherent eddies responds faster to the forcing (~3 months), than the co-
 30 herent eddy amplitude (which is lagged by ~6 months). Regional analysis ... Our anal-
 31 ysis highlights the relative importance of the coherent eddy field in the ocean kinetic en-
 32 ergy budget, implies a strong response of the eddy number and eddy amplitude to forc-
 33 ing at different time-scales, and showcases the seasonality, and multidecadal trends of
 34 coherent eddy properties.

35 **Plain language summary**

36 Coherent eddies are the most common feature ~~in the oceans~~ of ocean variability
 37 observable from satellites. They are crucial in ocean dynamics as they can transport prop-
 38 erties over long distances and interact with the atmosphere. Our study investigates the
 39 seasonal, interannual, and long-term changes in the abundance and intensity of coher-
 40 ent eddies, by automatically identifying individual eddies over the available satellite al-
 41 timeter record. The seasonal cycle suggests a transition from numerous, smaller, and weaker
 42 coherent eddies, to fewer and larger, and stronger coherent eddies over the season. In
 43 addition, a long-term adjustment of the coherent eddy field is identified ~~possible due with~~
 44 possible links to long-term changes in the climate system.

45 1 Introduction

46 Mesoscale ocean variability with spatial scales of tens to hundreds of kilometers is
 47 comprised of processes such as vortices, waves, and jets (Ferrari & Wunsch, 2009; Fu et
 48 al., 2010). These mesoscale processes are highly energetic, and they play a crucial role
 49 in the transport of heat, salt, momentum, and other tracers through the ocean (Wun-
 50 sch & Ferrari, 2004; Wyrtki et al., 1976; Gill et al., 1974). ~~Possibly, On of~~ the most rec-
 51ognizable and abundant ~~process observed from satellites is ocean processes observable~~
 52 ~~from space are~~ mesoscale vortices. Although mesoscale vortices are commonly referred
 53 to in ~~the~~ literature as “mesoscale eddies”, this term is also often used to describe the to-
 54 tal mesoscale ocean variability (the time-varying component of the mesoscale flow), thus,
 55 ~~here to avoid ambiguity~~ we will refer to mesoscale vortices as *coherent eddies*.

56 Coherent eddies are quasi-circular ~~geostrophic~~ currents. According to their rota-
 57 tional direction, the sea surface height anomaly within a coherent eddy can have a neg-
 58 ative or positive sea surface height anomaly (cold-core and warm-core coherent eddies,
 59 respectively). This characteristic sea surface height signature of coherent eddies has been
 60 utilized to ~~automatically~~ identify and track coherent eddies from satellite altimetry (~~Cui et al., 2020; Martínez-Me-~~
 61 ~~(e.g., Chelton et al., 2007; Faghmous et al., 2015; Ashkezari et al., 2016; Martínez-Moreno et al., 2019; Cui et al.,~~
 62 ~~).~~ Automated identification algorithms of coherent eddies have ~~shown revealed~~ their ubiq-
 63 uity in the oceans, with a predominant influence at hotspots of eddy activity such as ~~boundary~~
 64 ~~in boundary current~~ extensions and the Antarctic Circumpolar Current. In these regions,
 65 ~~Chelton et al. (2011) it has been~~ estimated that coherent eddies contribute around 40–
 66 50% of the ~~net~~ mesoscale kinetic energy (Chelton et al., 2011) and thus a significant frac-
 67 tion of the total kinetic energy (Ferrari & Wunsch, 2009). Although this ~~unique~~ estimate
 68 showcases the importance of the mesoscale coherent eddy field, the energy contained by
 69 coherent eddies was estimated by extracting the ~~geostrophic velocities within the detected~~
 70 ~~coherent eddies, thus total geostrophic velocity within the radius of each detected coherent~~
 71 ~~eddy; thus,~~ it is possible ~~it that this estimate~~ may contain energy from other processes.
 72 ~~Here we extend on this past work by reconstructing the surface imprint of~~
 73 ~~the coherent eddies ...~~ Coherent eddies are ~~not only abundant and may have a large~~
 74 ~~proportion of the surface kinetic energy budget, but abundant and energetic;~~ therefore
 75 they are also essential to ocean dynamics as concluded by many previous studies (~~Patel et al., 2020; Schubert et a-~~
 76 ~~(Hogg & Blundell, 2006; Siegel et al., 2011; Beron-Vera et al., 2013; Frenger et al., 2013, 2015; Pilo et al., 2015; So-~~

78 There is broad consensus that mesoscale eddy kinetic energy has a pronounced sea-
 79 sonal variability (Uchida et al., 2017; Kang & Curchitser, 2017; Qiu & Chen, 2004; Qiu, 1999)
 80 (Qiu, 1999; Qiu & Chen, 2004; Kang & Curchitser, 2017; Uchida et al., 2017). Several
 81 hypotheses have been proposed to explain this seasonality including: seasonal variations
 82 of atmospheric forcing (Sasaki et al., 2014), seasonality of the mixed layer depth (Qiu
 83 et al., 2014; Callies et al., 2015), seasonality of the intensity of barotropic instability (Qiu
 84 & Chen, 2004), the variability of the baroclinic instability due to the seasonality of the
 85 vertical shear (Qiu, 1999), and a seasonal lag of the inverse energy cascade (i.e. energy
 86 is transported between scales, from small to large; Arbic et al., 2013) in combination with
 87 the presence of a front in the mixed layer, which can lead to a seasonal cycle of the baro-
 88 clinic instability (Qiu et al., 2014). On one hand, processes such as barotropic and baro-
 89 clinic instabilities control the seasonality of coherent eddies in the ocean. On the other
 90 hand, recent studies using observations and eddy-permitting climate models suggest sev-
 91 eral long-term adjustments of the global ocean capable of long-term changes in the co-
 92 herent eddy field. Such readjustments include a multidecadal increase in the ocean strat-
 93 ification resulted resulting from temperature and salinity changes (Li et al., 2020), a hor-
 94 izontal readjustment of the sea surface temperature gradients (Ruela et al., 2020; Bouali et al., 2017;
 95 (Cane et al., 1997; Bouali et al., 2017; Ruela et al., 2020), and an intensification of the
 96 kinetic energy, eddy kinetic energy, and mesoscale eddy kinetic energy over the last 3 decades
 97 as a consequence of an increase in wind forcing (Hu et al., 2020; Wunsch, 2020; Martínez-
 98 Moreno et al., 2021). All these seasonal factors and long-term readjustments directly in-
 99 fluence the annual and decadal response of the coherent eddy field, however, the season-
 100 ality of the coherent component of the eddy kinetic energy, as well as the seasonal cy-
 101 cle and trends of the coherent eddy statistics, remain unknown.

102 Here we present a new global climatology of the coherent eddy kinetic energy by
 103 reconstructing the coherent eddy signature from satellite observations. Our study doc-
 104 uments the seasonal cycle of the coherent eddy kinetic energy, and the seasonal cycle and
 105 long-term trends of the coherent eddy properties over the satellite record. Moreover, we
 106 conduct more detail analysis detailed analyses in regions where coherent eddies domi-
 107 nate the eddy kinetic energy field. This The rest of this paper is structured as follows:
 108 the data sources and methodology are described in section Section 2. Then, we present
 109 the climatology, energy ratios, and global seasonality of the coherent eddy kinetic en-
 110 ergy in section Section 3. Section 4 presents outlines the global climatology and season-

111 ability of coherent eddy properties, followed by long-term changes of the coherent eddy prop-
 112 erties (~~section~~Section 5). Then we focus our attention on the seasonal cycle and coher-
 113 ent eddy properties in regions dominated by coherent eddies (~~section~~Section 6). Finally,
 114 ~~section~~Section 7 summarizes the main results and discusses the implications of this study.

115 **2 Methods**

116 We use daily sea surface height (SSH) data made available by the Copernicus Ma-
 117 rine Environment Monitoring Service in near real time (CMEMS, 2017). This gridded
 118 product contains the sea surface height and geostrophic velocities with daily 0.25° res-
 119 olution from January 1993 to 2019. The daily geostrophic velocities ~~allowed~~allow us to
 120 compute the kinetic energy (KE) and eddy kinetic energy (EKE) over the satellite record.
 121 The main source of EKE is the time-varying wind (Ferrari & Wunsch, 2009), ~~thus we computed~~
 122 ; thus, we also compute the seasonal cycle of the wind magnitude from the JRA55 re-
 123 analysis (Japan Meteorological Agency, Japan, 2013) using wind velocities at 10m above
 124 the ocean's surface.

125 Over the same record, coherent eddy statistics from Martínez-Moreno et al. (2019),
 126 hereafter ~~M-MM19~~, are analyzed and compared ~~to~~with those released by Chelton &
 127 Schlax (2013), ~~both~~hereafter CS13. ~~Both~~ datasets are gridded in a 1° resolution ~~-Although~~
 128 ~~both datasets and~~ are produced via automated eddy identification algorithms using closed
 129 contours of SSH. ~~However~~, these datasets have important differences in the criteria they
 130 use to identify and record coherent eddies statistics. The major differences include:
 131 ~~M-MM19~~'s algorithm requires an adjustment between a 2D Gaussian and the SSH anomaly
 132 (SSHa) surface within the ~~identify identified~~ closed contour, while ~~Chelton~~CS13's only
 133 uses the ~~outer-most~~outermost closed contour of SSH; (ii) ~~M-MM19~~'s dataset reports
 134 the maximum SSHa within the identified coherent eddy, while ~~Chelton~~CS13's algorithm
 135 reports the maximum SSH value minus the discrete level in which the coherent eddy was
 136 identified; ~~M-M and~~ (iii) ~~MM19~~'s dataset includes all detected coherent eddies, while ~~Chelton~~CS13's
 137 dataset excludes (iii) coherent eddies with lifetimes shorter than four weeks and (iv) co-
 138 herent eddy amplitudes smaller than 1cm. Moreover, ~~M-MM19~~'s algorithm allows the
 139 reconstruction of the coherent eddy field under the assumption that coherent eddies have
 140 a 2D Gaussian imprint in the sea surface height. This Gaussian reconstruction of the co-
 141 herent eddy field then ~~allow~~allows us to estimate the coherent geostrophic eddy veloc-
 142 ities and thus the kinetic energy contained only by coherent eddies.

143 **2.1 Kinetic Energy decomposition**

Kinetic energy is commonly divided into the mean and time-varying components through a Reynolds decomposition. At a given time, the surface velocity field $\mathbf{u} = (u, v)$ is split into the time mean ($\bar{\mathbf{u}}$) and time varying components (\mathbf{u}'). Moreover, [M-M-MM19](#) proposed to further decompose the eddy kinetic energy into the energy contained by coherent features (\mathbf{u}'_e) and non-coherent features (\mathbf{u}'_n). Therefore the KE equation can be written as:

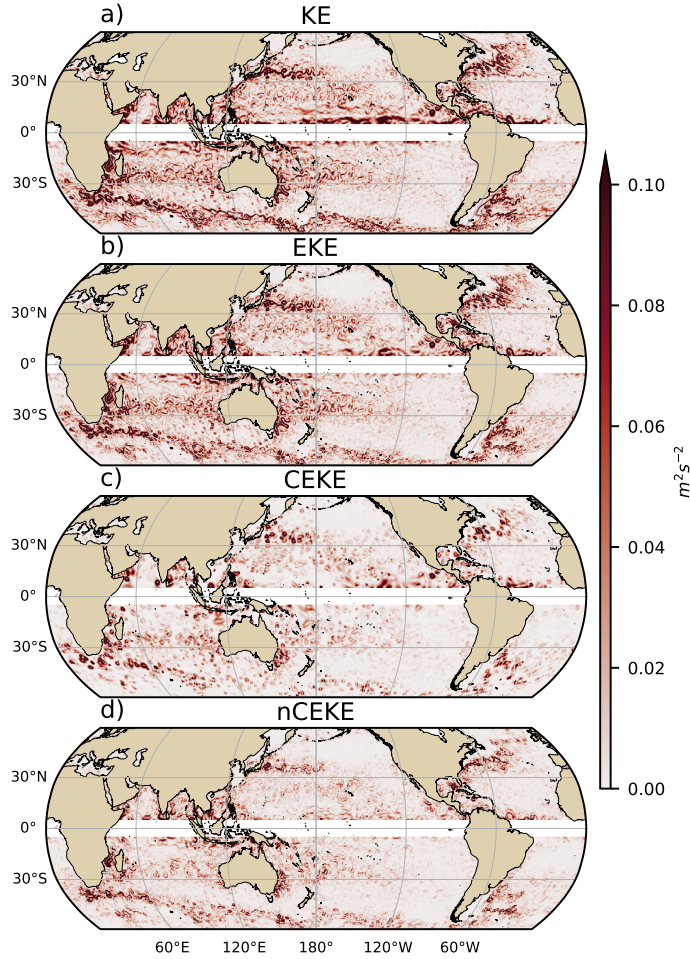
$$\text{KE} = \underbrace{\bar{u}^2 + \bar{v}^2}_{\text{MKE}} + \underbrace{u'^2_e + v'^2_e}_{\text{CEKE}} + \underbrace{u'^2_n + v'^2_n}_{\text{nCEKE}} + \mathcal{O}_c^2 + \mathcal{O}^2 \quad (1)$$

Due to the properties of this decomposition, the second order term \mathcal{O}^2 is zero when averaged over the same period as $\bar{\mathbf{u}}$. However, \mathcal{O}_c^2 is not [necessarily necessarily](#) negligible, unless it is averaged over time and space. More information about the decomposition of the field into coherent features and non-coherent features is explained [by in](#) Martínez-
Moreno et al. (2019). A global snapshot of each component of kinetic energy decomposition is shown in Figure 1, where the KE and EKE are comprised of rings and filaments. As expected, the decomposition of EKE into CEKE and nCEKE components [exhibit exhibits](#) only ring-like signatures expected of coherent eddies, while the non-coherent component shows [filaments and some miss-identified primarily filaments, with some mis-identified](#) coherent eddies.

163 **2.2 Eddy statistics**

The eddy statistics used in this study include (i) the eddy count ($cEddy_n$) defined as the number of [coherent](#) eddies per grid cell, (ii) the eddy diameter defined as the diameter of a circle with equal area [as to](#) the closed contour of each identified eddy, and (iii) the mean eddy amplitude defined as the mean amplitude of the coherent eddies within the cell ($cEddy_{amp}$). The latter metric can be separated into positive ($cEddy_{amp}^+$) and negative ($cEddy_{amp}^-$) coherent eddy amplitudes, defined as the mean amplitude of warm core and cold core coherent eddies, respectively, within the cell. The polarity independent eddy amplitude ($|cEddy_{amp}|$) is defined as:

$$|cEddy_{amp}| = \frac{1}{2} (cEddy_{amp}^+ - cEddy_{amp}^-) \quad (2)$$



160 **Figure 1.** Snapshot of surface kinetic energy ($\overline{\text{KE}}$), surface eddy kinetic energy ($\overline{\text{EKE}}$),
 161 surface coherent eddy kinetic energy ($\overline{\text{CEKE}}$), and surface non-coherent eddy kinetic energy
 162 ($\overline{\text{nCEKE}}$) for the 1st of January 2017.

172 Note that the cEddy_{amp}^+ and cEddy_{amp}^- are sign definite, thus the difference will always
 173 be positive, whereas the gridded averaged cEddy_{amp} can be negative or positive noting
 174 the dominant polarity of coherent eddies in the region, and the absolute cEddy_{amp} is de-
 175 noted by $\text{cEddy}_{|amp|}$. We analyze the climatology, seasonal cycles and trends of the eddy
 176 statistics above eddy statistics over the available satellite record, namely between 1993
 177 and 2019. We exclude the equatorial region (10°S - 10°N) and regions poleward of 60° ,
 178 because the geostrophic approximation is invalid near the equator and the
 179 satellite spatial coverage at high-latitudes is unable to resolve the coherent
 180 eddy scales polewards of 60° . Note that the climatology of cEddy_n is computed by

181 adding all the identified eddies over the record, while all other climatological statistics
 182 are computed as the time-average over the record. Seasonal climatologies are calculated
 183 for the monthly average of each coherent eddy statistic, while hemispherical time-series
 184 are filtered with a running average of 90 days. Trends of $cEddy_n$ and $|cEddy_{amp}|$ are cal-
 185 culated by coarsening the dataset to a 5° grid, and then linear trends are computed for
 186 each grid point, ~~the statistical significance~~. The statistical significance of trends is as-
 187 sessed by a modified Mann-Kendall test (Yue & Wang, 2004).

188 Time averages are denoted by $\overline{}$, while area-weighted averages are denoted using
 189 $\langle \rangle$, ~~the area weighted of where the area-weighted average of a function f is:~~

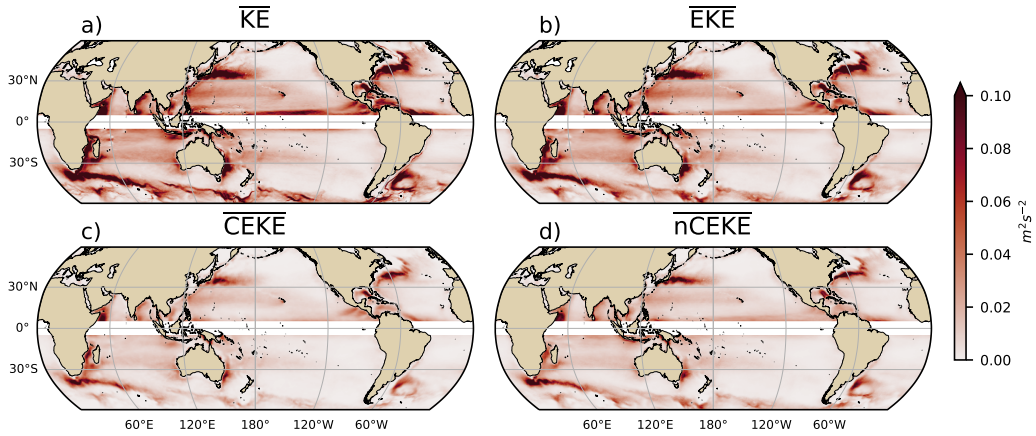
$$\langle f \rangle = \frac{\int f dx dy}{\int dx dy} \frac{\int f \xi dx dy}{\int \xi dx dy}, \quad (3)$$

190 ~~area-weighted coherent eddy properties masked areas each time, Where ξ is a mask that~~
 191 ~~is set to zero in grid cells~~ where no coherent eddies were identified.

192 3 Global Coherent Eddy Energetics

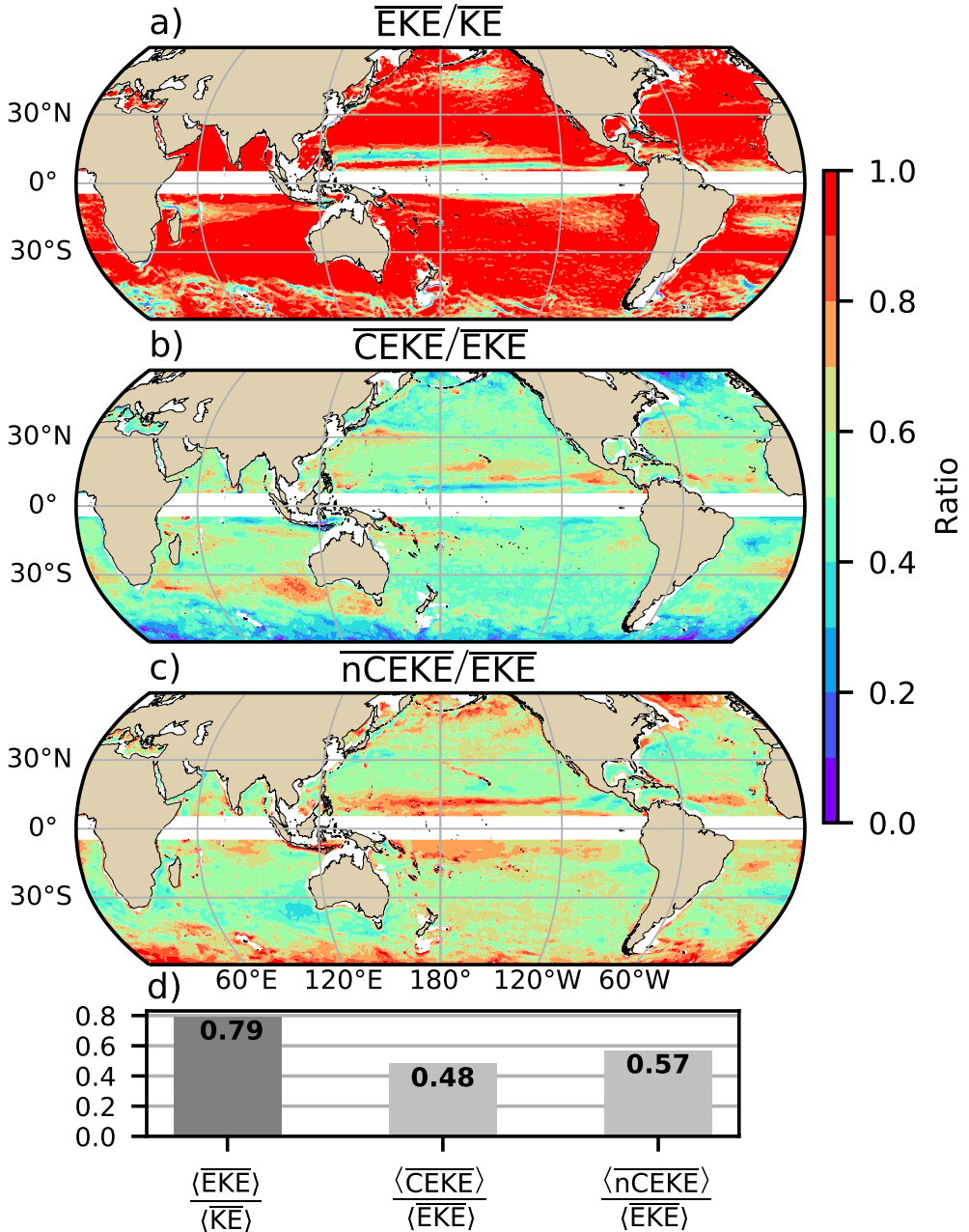
193 The kinetic energy decomposition estimated from sea surface height measured by
 194 satellite altimeters averaged from 1993-2019 is shown in Figure 2. These maps show that
 195 many regions of the global ocean are highly energetic in mean KE (\overline{KE}), mean EKE (\overline{EKE}),
 196 mean coherent eddy kinetic energy (\overline{CEKE}) and mean non-coherent eddy kinetic energy
 197 (\overline{nCEKE}). The spatial pattern highlights ~~well known well-known~~ regions of the ocean
 198 where mesoscale processes are abundant, such as the western boundary ~~extensions current~~
 199 ~~extensions (WBCe)~~ and the Antarctic Circumpolar Current. ~~Remarkably, the The~~ spa-
 200 tial distribution of the energy contained by the reconstructed mesoscale coherent eddies
 201 and non-coherent components are similar (Figures 2c,d). However, there are some re-
 202 gions where coherent eddies dominate over non-coherent, and vice-versa. Overall, this
 203 decomposition ~~suggest suggests~~ that boundary current extensions and other energetic
 204 regions ~~, in particularly , of the ocean, particularly~~ eddy-rich regions ~~in the ocean~~ con-
 205 tain both coherent and non-coherent components of the kinetic energy.

218 Eddy kinetic energy is known to be more than an order of magnitude greater than
 219 ~~kinetic energy of the mean flow (MKE(Gill et al., 1974); Gill et al. 1974)~~; this result
 220 is clearly shown in Figure 3a, where \overline{EKE} is responsible for almost all the \overline{KE} across the
 221 ocean, except for regions with persistent currents over time. Such regions are located in
 222 the mean boundary extension locations, the equatorial Pacific currents and regions in



206 **Figure 2.** Mean surface kinetic energy (\overline{KE}), surface eddy kinetic energy (\overline{EKE}), surface
207 coherent eddy kinetic energy (\overline{CEKE}), and surface non-coherent eddy kinetic energy (\overline{nCEKE})
208 averaged between 1993-2018.

223 the Antarctic Circumpolar Current, where the \overline{EKE} explains around 40% of the \overline{KE} . In
224 a previous study, Chelton et al. (2011) estimated that the EKE within coherent eddies
225 with lifetimes greater than 4 weeks contain between ~~40 to 60 percent~~ 40-60% of the \overline{EKE} .
226 Our method to reconstruct the coherent eddy signature (Figure 3b) further corroborates
227 that the coherent eddy component ($\langle \overline{CEKE} \rangle$) has \sim 48% of the $\langle \overline{KE} \rangle$ (Figure 3d). Fur-
228 thermore, global area averages of the ratios show that $\langle \overline{EKE} \rangle$ explains \sim 78% of the ocean
229 $\langle \overline{KE} \rangle$ field, while non coherent eddy features contain \sim 57% percent of the $\langle \overline{EKE} \rangle$. Note
230 that the globally averaged coherent and non coherent components do not add to 100%
231 as the cross terms (\mathcal{O}_c^2) are non-zero, ~~due to and~~ coherent eddy reconstruction errors.
232 The spatial pattern reveals a dominance of the \overline{CEKE} equatorward from the boundary
233 ~~extensions and current extensions and in~~ areas with large coherent eddy contributions
234 of around 80% of the region's eddy kinetic energy ~~can be found, such as~~ south of Aus-
235 tralia, in the Tehuantepec Gulf, and in the tropical Atlantic. An evident signal is an a
236 reduction of the energy contained by coherent eddies at high latitudes and an increase
237 in the energy explained by non-coherent eddies; this signal could be a consequence of the
238 ~~incapability inability~~ of the 0.25° satellite resolution (~ 13 km at 60° latitude) to resolve
239 coherent eddies with scales smaller than ~ 10 km (first baroclinic Rossby radius at 60° ;
240 Chelton et al. 1998).



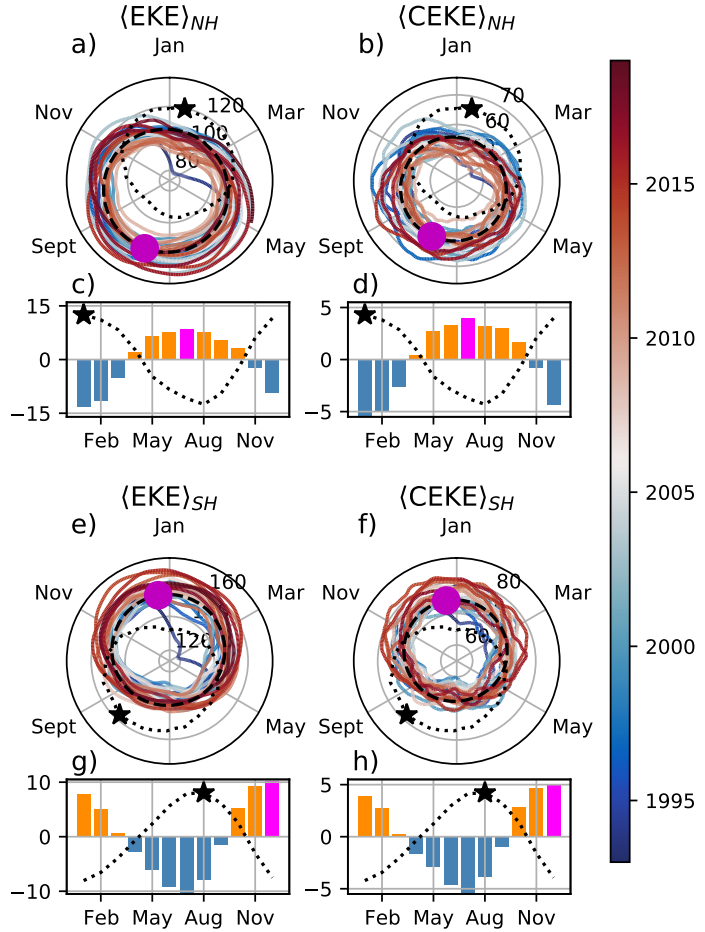
209 **Figure 3.** Ratios of the kinetic energy components. a) Map of the proportion of mean eddy
 210 kinetic energy (\overline{EKE}) versus mean kinetic energy (\overline{KE}); b) Map of the percentage of mean co-
 211 herent eddy kinetic energy (\overline{CEKE}) versus mean eddy kinetic energy (\overline{EKE}); c) Map of the
 212 percentage of mean non-coherent eddy kinetic energy (\overline{nCEKE}) versus mean eddy kinetic energy
 213 (\overline{EKE}); d) Global time and area averaged (represented by $\langle \rangle$) percentage of mean eddy kinetic
 214 energy ($\langle \overline{EKE} \rangle$) versus the global mean kinetic energy ($\langle \overline{KE} \rangle$), area averaged percentage of mean
 215 coherent eddy kinetic energy ($\langle \overline{CEKE} \rangle$) and mean non coherent eddy kinetic energy ($\langle \overline{nCEKE} \rangle$)
 216 versus global mean eddy kinetic energy ($\langle \overline{EKE} \rangle$). Regions where the depth of the ocean is shall-
 217 lower than 1000m are removed from the ratio estimation.

Figure 4 shows the seasonal cycle of the area weighted EKE and CEKE for the Northern Hemisphere ($\langle \text{EKE} \rangle_{NH}$ and $\langle \text{CEKE} \rangle_{NH}$; 10°N - 60°N) and Southern Hemisphere ($\langle \text{EKE} \rangle_{SH}$ and $\langle \text{CEKE} \rangle_{SH}$; 60°S - 10°S). In both hemispheres, the $\langle \text{EKE} \rangle$ and $\langle \text{CEKE} \rangle$ peak during summer. In the Northern Hemisphere, the largest $\langle \text{EKE} \rangle_{NH}$ and $\langle \text{CEKE} \rangle_{NH}$ occurs in July, ~ 6 months after the maximum winds in January (purple bar and back star in Figure 4c and d). Meanwhile, the Southern Ocean $\langle \text{EKE} \rangle_{SH}$ and $\langle \text{CEKE} \rangle_{SH}$ seasonal maxima arises during December, ~ 4 months after the maximum winds in August (purple bar and back star in Figure 4g, and h). This lag between winds and the eddy and coherent eddy energy components is further discussed in section 4.

The cyclic plots in Figure 4 show the temporal evolution of $\langle \text{EKE} \rangle$ and $\langle \text{CEKE} \rangle$. Note that high frequency variability can be observed in the $\langle \text{CEKE} \rangle$ field with temporal scales of a few months, this variability could be attributed to regional dynamics averaged over the hemisphere ~~-(boundary currents, ocean gyres, etc.)~~, as well as errors within the coherent eddy reconstruction. Additionally, concentric changes in the cyclic plots highlight long-term changes over the record. For example, the Northern Hemisphere winters ~~in~~during early years of the record (blue) had a more energetic coherent eddy field, which has transitioned to weaker coherent energy ~~contents~~content since 2010 (red), in other words, the intensity of the $\langle \text{CEKE} \rangle_{NH}$ field has decreased. A larger long-term change can be observed in the Southern Hemisphere, where concentric growth over time in $\langle \text{EKE} \rangle_{SH}$ and $\langle \text{CEKE} \rangle_{SH}$ support the previously observed strengthening of the eddy field in the Southern Ocean (Hogg et al., 2015; Martínez-Moreno et al., 2019; Martínez-Moreno et al., 2021).

4 Global Coherent Eddy Statistics

Coherent eddy kinetic energy allows us to quantify and study the energy of the eddy field, but the coherent eddy properties computed by automated coherent eddy identification algorithms allow us to further investigate in more detail the contribution and temporal changes of their abundance (*i.e.* the number of eddies) and their intensity (both their amplitude and diameter). Figure 5 shows gridded climatologies of the number of eddies and the eddy amplitude. ~~We contrast our M-M~~In this analysis, we contrast our MM19 eddy count with ~~Chelton et al. (2007)~~(that of CS13 (Chelton et al., 2007; Figure 5a-b)). Although the number of the identified eddies is larger in M-M~~MM19~~, possibly due to the lifespan filter implemented by ~~Chelton~~CS13, both datasets reveal consis-



263 **Figure 4.** Seasonality of the area-weighted eddy kinetic energy ($\langle EKE \rangle$) and
264 coherent eddy kinetic energy ($\langle CEKE \rangle$). Panels a) and b) show the time-series of the North-
265 ern Hemisphere, while panels e) and f) correspond to the Southern Hemisphere. Panels c) and
266 d) show the seasonal cycle of the $\langle EKE \rangle_{NH}$ and $\langle CEKE \rangle_{NH}$ in the Northern Hemisphere, and
267 panels g) and h) show the Southern Hemisphere ($\langle EKE \rangle_{SH}$ and $\langle CEKE \rangle_{SH}$). Dashed lines cor-
268 respond to the seasonal cycle of the fields and dotted lines show the seasonal cycle of the wind
269 magnitude smoothed over 120 days (moving average). The black and magenta markers (circle
270 and bar) show the maximum of the seasonal cycle for the kinetic energy components and the
271 wind magnitude, respectively. In the cyclic plots, line colors shows the year.

tent spatial patterns. For example, both datasets show high abundance of eddies in the East North Pacific, East North Atlantic, as well as the East South Pacific, East South Atlantic and East Indian Ocean, and ~~small number counts of fewer~~ eddies in the tropics and ~~in high at higher~~ latitudes ($\sim 60^\circ$). An interesting pattern also emerges in both eddy count datasets, where small scale structures ~~with larger eddy counts are favored across the ocean. In addition, to preferential emerge in the eddy count field. These small structures highlight preferred~~ coherent eddy paths observable in boundary ~~extensions and regions in current extensions and over regions of~~ the Southern Ocean. These ~~elusters~~ structures and paths of coherent eddies could be associated with topographic features, ~~however they remain a puzzling with overall~~ consistency between the eddy count ~~pattern using these two patterns using the two different~~ eddy identification methods.

Regions with large counts of eddies have in general small absolute amplitudes (Figure 5 c),~~. The~~ ocean gyre interiors ~~follow with have~~ a larger absolute amplitude and finally regions such as the boundary ~~extensions and current extensions and the~~ Antarctic Circumpolar Current have the largest coherent eddy absolute amplitudes~~as shown~~, ~~as shown also~~ by Chelton et al. (2011). Eddy amplitude highlights regions dominated by a given coherent eddy polarity, for example, boundary extensions have a preferred sign (Figure 5 d); ~~namely,~~ positive amplitude polewards of the boundary ~~current~~ extension mean location, and negative amplitude equatorwards. This sign preference is consistent with the preferential way ~~that~~ coherent eddies are shed from boundary ~~extensions; current extensions; with~~ warm core eddies (positive) polewards of the boundary current extension, and equatorward for cold core eddies (negative) (Kang & Curchitser, 2013; Chelton et al., 2011, 2007). These global statistics reveal the absolute coherent eddy amplitude ~~is a proxy of as a proxy for~~ the CEKE with similar spatial patterns (Figure 2 & Figure 5c) and showcases that regions where $\overline{\text{CEKE}}$ has a large proportion of $\overline{\text{EKE}}$ (Figure 3), the absolute coherent eddy amplitude is also large.

To further understand the seasonal cycle of $\langle \text{CEKE} \rangle$, we compute the climatology of coherent eddy properties in each hemisphere (Figure 6). The seasonality of the number of eddies in the Northern Hemisphere peaks ~~on-in~~ April (Figure 6-a, c), while the Southern Hemisphere maximum number of eddies occurs during October (Figure 6-e, g). Meanwhile, the seasonality of the ~~polarity independent~~ eddy amplitude ($\langle |c\text{Eddy}_{amp}| \rangle$) peaks in August and January for the Northern and Southern Hemispheres respectively (Figure 6-b, d, f, and h). As expected, the seasonality of $\langle |c\text{Eddy}_{amp}| \rangle$ ~~xw, or~~ equivalents

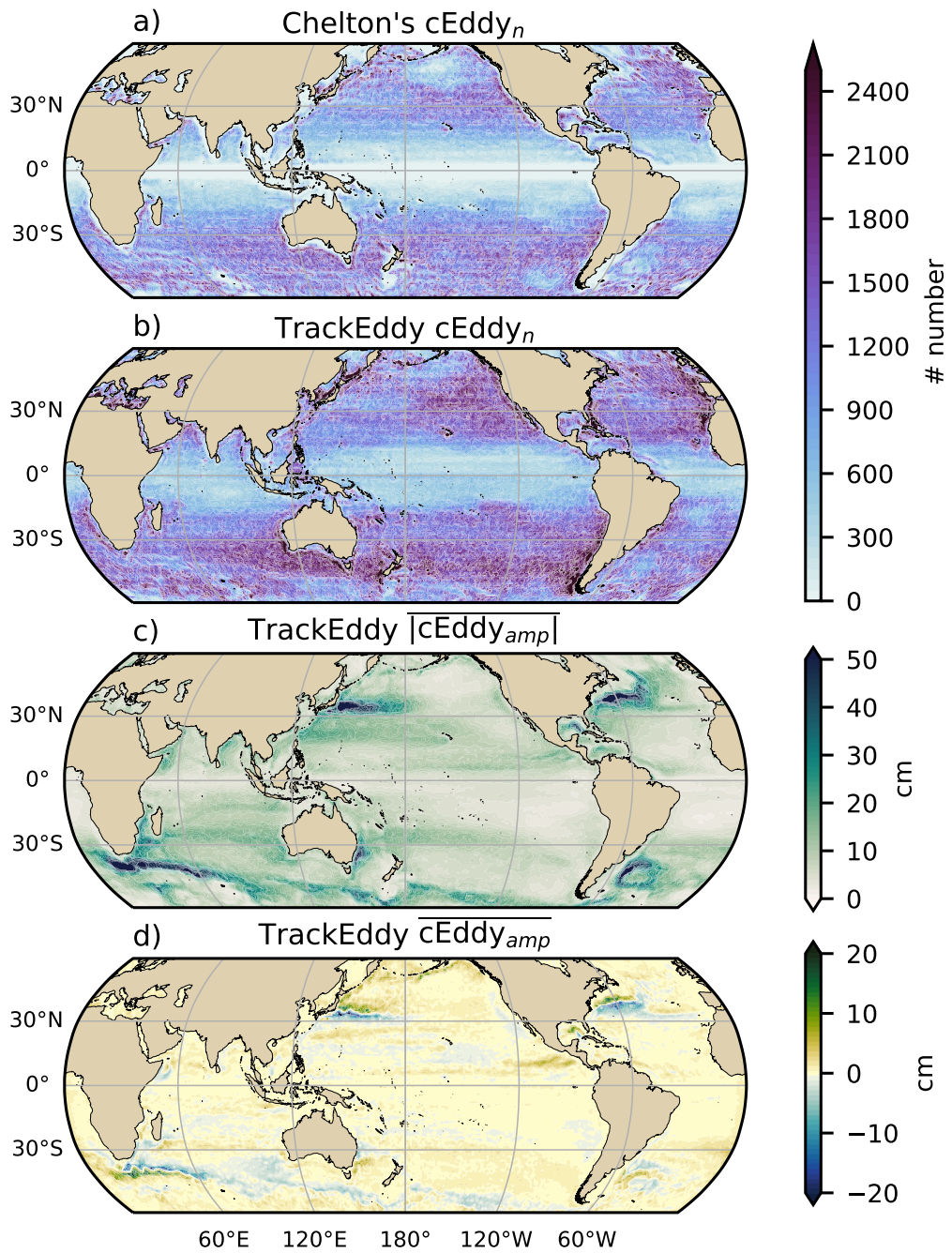


Figure 5. Averaged coherent eddy statistics. a) Climatology of the number of coherent eddies ($cEddy_n$) identified by Chelton et al. (2007); b) Climatology of the number of coherent eddies ($cEddy_n$) identified by Martínez-Moreno et al. (2019); c) Climatology of the mean absolute coherent eddy amplitude ($cEddy_{amp}$). d) Climatology of the mean coherent eddy amplitude ($cEddy_{amp}$).

320 lent to the intensity of the coherent eddies, is consistent with the seasonal cycle of $\langle \text{CEKE} \rangle$.
 321 ~~Furthermore,~~

322 ~~A key feature of Figure 6 is~~ a distinct lag of ~ 3 months ~~is observed~~ between the
 323 winds and eddy count, while the eddy amplitude maximum occurs ~ 6 months after the
 324 seasonal maxima in winds. We ~~observe suggest that~~ the eddy number increases earlier
 325 in the year and ~~through~~ through eddy-eddy interactions (merging of coherent eddies), ~~the~~ the am-
 326 plitude of the coherent eddy increases ~ 3 months after. This seasonal lag and summer
 327 maxima is consistent with ~~Figure 5, furthermore, previous studies~~ ~~previous studies which~~
 328 suggest that a time-lag of the inverse cascade (Sasaki et al., 2014; Qiu et al., 2014) is re-
 329 sponsible ~~of for~~ for the EKE seasonal cycle, where winter has the highest energy at the small-
 330 est scales (non-resolvable with satellite observations), spring and autumn have the high-
 331 est and lowest energy ~~in at~~ at scales of 50-100 km, and summertime has the highest energy
 332 at the largest scales (> 100 km; Uchida et al. 2017). Thus, the maximum of $\langle \text{EKE} \rangle$, $\langle \text{CEKE} \rangle$,
 333 and $\langle |c\text{Eddy}_{amp}| \rangle$ located during summertime ~~suggest suggests~~ that the seasonality of
 334 eddies and coherent eddies could be dominated by scales larger than 100 km.

335 This result can be further explored by looking at the seasonal evolution of the eddy
 336 diameter ($c\text{Eddy}_d$). Note that 90% of identified coherent eddies have diameters between
 337 50 to 220 km (Figure 7-a). We ~~divided partition~~ eddies into large-scale coherent eddies
 338 (diameter > 120 km) and small-scale coherent eddies (diameter < 120 km; Figure 7a).
 339 In the Northern Hemisphere, ~~small small-scale~~ eddies have a seasonal peak in diameter
 340 during May, while ~~large large-scale~~ eddies have the greatest diameter in September (Fig-
 341 ure 7-b). Meanwhile, in the Southern Hemisphere, the small-scale coherent eddies ~~have~~
 342 ~~the exhibit~~ maximum diameter in December, while ~~the diameter of~~ large-scale coherent
 343 eddies ~~peak peaks~~ in February (Figure 7 c). This result suggests that wind driven baro-
 344 clinic instabilities generate small coherent eddies early in the season, which then merge
 345 and grow to become larger in diameter and amplitude, and thus, more energetic. This
 346 process is ~~likely~~ associated with the inverse energy cascade, and ~~suggest suggests~~ that
 347 this mechanism not only drives ~~the~~ EKE seasonality, but also may be responsible ~~of for~~
 348 the seasonal cycle of coherent eddies.

349 Long-term changes can be observed in Figure 6a,b, e, and f where ~~growing shrinking~~
 350 ~~growing/shrinking~~ concentric circles over time denote an ~~increase decrease increase/decrease~~
 351 trend of the field. This trend is particularly evident in the Southern Hemisphere, where

352 the number of eddies has decreased, while the eddy amplitude has increased. This re-
 353 sult is consistent with the observed trends in EKE and mesoscale EKE in the Southern
 354 Ocean (Hogg et al., 2015; Martínez-Moreno et al., 2019).

355 ~~Seasonality of the area-weighted eddy kinetic energy ($\langle EKE \rangle$), coherent eddy kinetic
 356 energy ($\langle CEKE \rangle$). Panels a and b show the time-series of the Northern Hemisphere, while
 357 panels e and f correspond to the Southern Hemisphere. Panels c and d show the seasonal
 358 cycle of the $\langle EKE \rangle_{NH}$ and $\langle CEKE \rangle_{NH}$ in the Northern Hemisphere, and panels g and
 359 h show the Southern Hemisphere ($\langle EKE \rangle_{SH}$ and $\langle CEKE \rangle_{SH}$). Dashed lines correspond
 360 to the seasonal cycle of the fields and dotted lines show the seasonal cycle of the wind
 361 magnitude smoothed over 120 days (moving average). The black and magenta markers
 362 (circle and bar) show the maximum of the seasonal cycle for the kinetic energy components
 363 and the wind magnitude, respectively. In cyclic plots, line colors shows the year.~~

364 ~~Seasonality of the count of number of eddies ($eEddy_n$) and area-weighted polarity
 365 independent coherent eddy amplitude ($\langle eEddy_{amp} \rangle$); Panels a and b show the time-series
 366 of the Northern Hemisphere, while panels e and f correspond to the Southern Hemisphere.
 367 Panels c and d show the seasonal cycle of the $eEddy_n$ and $\langle |eEddy|_{amp} \rangle_{NH}$ in the Northern
 368 Hemisphere, and panels g and h show the Southern Hemisphere ($eEddy_n$ and $\langle |eEddy|_{amp} \rangle_{SH}$).
 369 Dashed lines correspond to the seasonal cycle of the fields and dotted lines show the seasonal
 370 cycle of the wind magnitude smoothed over 120 days (moving average). The black and
 371 magenta markers (circle and bar) show the maximum of the seasonal cycle for the eddy
 372 property and the wind magnitude, respectively. In cyclic plots, line colors shows the year.~~

373 ~~Distribution of the identified eddy diameter ($eEddy_d$; km) and hemispherical seasonality
 374 of the coherent eddy diameter. a) Distribution in percentage of identified eddy amplitude,
 375 solid bar below distribution represents 90% of the identified eddies. Seasonal cycle of
 376 the eddy diameter for the b) Northern Hemisphere and c) Southern Hemisphere. Dark
 377 solid line and area corresponds to coherent eddies with diameters larger than 120 km,
 378 while light gray dash-dotted line and area shows coherent eddies with diameters smaller
 379 than 120 km.~~

380 The coherent eddy amplitude from positive coherent eddies and negative coherent
 381 eddies show similar seasonal cycles to the absolute eddy amplitude. The Northern Hemis-
 382 phere decrease in absolute eddy amplitude is driven by a decrease of the amplitude of
 383 negative coherent eddies in the Northern Hemisphere. Meanwhile in the Southern Ocean,

384 the increase in absolute eddy amplitude is corroborated by ~~an-a~~ strengthening of both
 385 coherent eddy polarities since the early 90s.

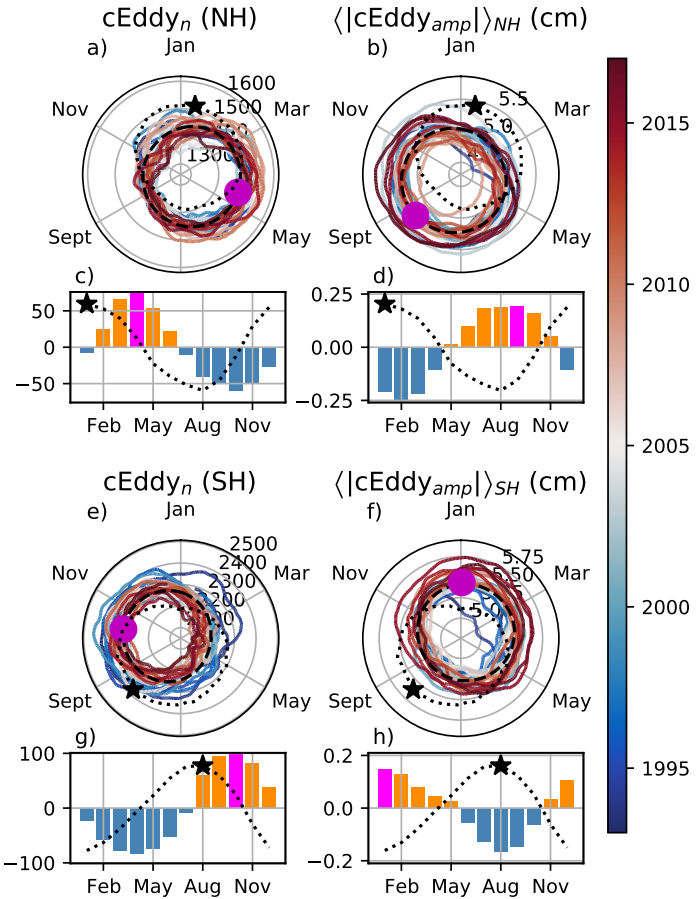
402 **5 Trends**

403 The results presented in Figures 4 and 6 suggest a long-term readjustment of the
 404 coherent eddy field. The long-term trends of the number of coherent eddies, absolute co-
 405 herent eddy amplitude, and coherent eddy amplitude polarities are further explored in
 406 Figure 8 . ~~Chelton's and M-M contrasting the MM19 and CS13 methods. MM19 and~~
 407 CS13 datasets show consistent spatial patterns in the trends and significance of the num-
 408 ber of coherent eddies and the absolute coherent eddy amplitude. Several regions in the
 409 ocean, such as the Southern Ocean, North Atlantic and North Pacific, show a decrease
 410 in the number of eddies. Those same regions also have a clear increase in the absolute
 411 coherent eddy amplitude. These trends are similar to those observed in mesoscale eddy
 412 kinetic energy (Martínez-Moreno et al., 2021) and provide additional evidence of a read-
 413 justment of the mesoscale eddy field over the last 3 decades.

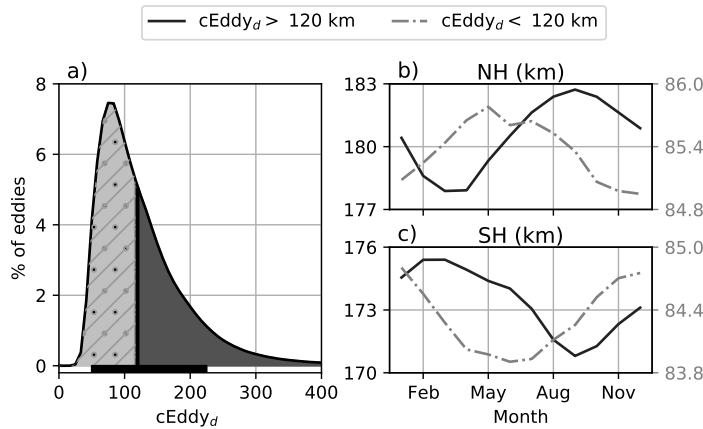
414 ~~@Matt: What do you think? Is it important to highlight the trends we observe are different to sea level rise?~~

415

416 The observed trends of $cEddy_{amp}$ in several oceanic regions have the same scale
 417 as sea level rise ($\sim 3\text{cm}$ per decade)~~by~~. By analyzing the positive and negative coher-
 418 ent eddy amplitude~~we can discard~~, we filter out the observed trends ~~correspond to an~~
 419 that come from a net increase in sea level. In fact, each coherent eddy polarity has in-
 420 tensified in the Southern Ocean and North East Pacific and Atlantic. In other words,
 421 the amplitude of each polarity has increased over time, and thus this strengthening is
 422 an intrinsic response of the coherent eddy field. Note that the negative coherent eddy
 423 amplitude dominates the global $|cEddy_{amp}|$ trends (Figure 8e, f). However, different trend
 424 ~~pattern~~patterns can be observed in both positive and negative coherent eddy amplitudes
 425 in the ~~north Atlantic and north~~North Atlantic and North Pacific, where the negative
 426 coherent eddy amplitude in the Western Boundary Currents appears to decrease.



386 **Figure 6.** Seasonality of the count of number of eddies ($c\text{Eddy}_n$) and the area-weighted
 387 polarity independent coherent eddy amplitude ($\langle |c\text{Eddy}_{amp}| \rangle$); Panels a and b show the
 388 time-series of the Northern Hemisphere, while panels e and f correspond to the Southern
 389 Hemisphere. Panels c and d show the seasonal cycle of the $c\text{Eddy}_n$ and $\langle |c\text{Eddy}_{amp}| \rangle_{NH}$ in
 390 the Northern Hemisphere, and panels g and h show the Southern Hemisphere $c\text{Eddy}_n$ and
 391 $\langle |c\text{Eddy}_{amp}| \rangle_{SH}$. Dashed lines correspond to the seasonal cycle of the fields and dotted lines
 392 show the seasonal cycle of the wind magnitude, smoothed over 120 days (moving average). The
 393 black and magenta markers (circle and bar) indicate the maximum of the seasonal cycle for the
 394 eddy property, and the wind magnitude, respectively. In the cyclic plots, line colors show the
 395 year from 1993-2019.



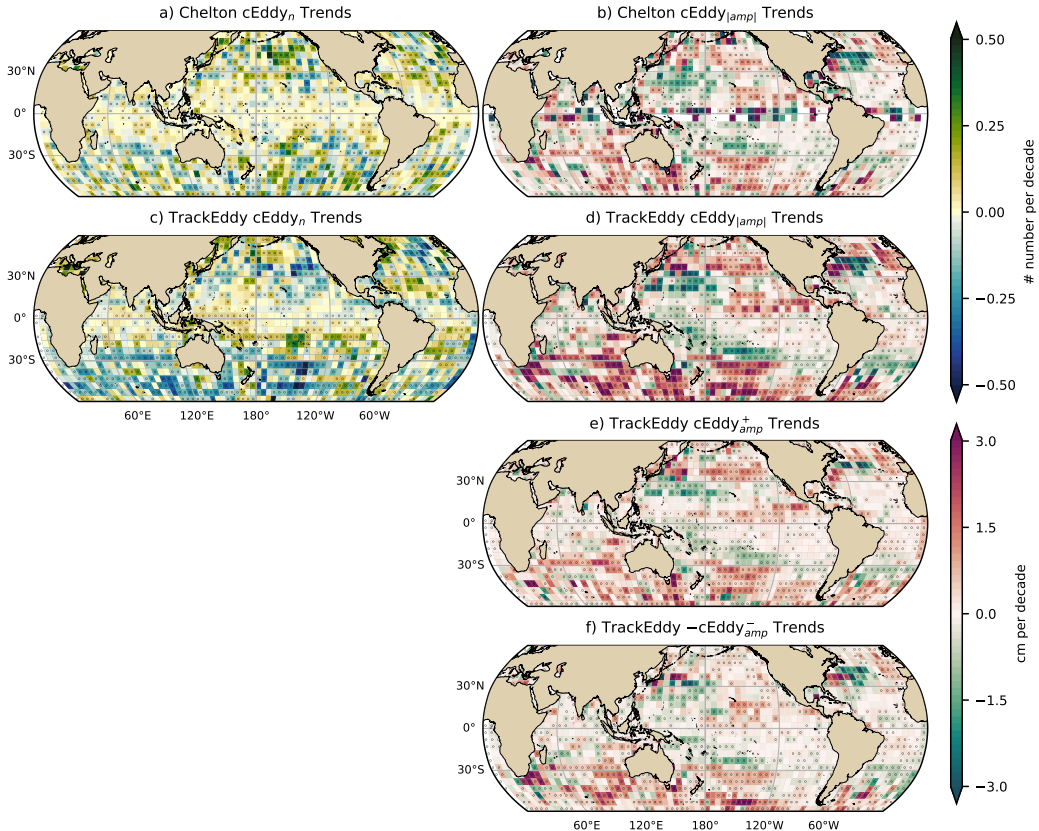
396 **Figure 7.** Distribution of the identified eddy diameter ($cEddy_d$; km) and hemispherical
 397 seasonality of the coherent eddy diameter. a) Distribution in percentage of identified eddy
 398 amplitude, solid bar below distribution represents 90% of the identified eddies. Seasonal cycle
 399 of the eddy diameter for the b) Northern Hemisphere and c) Southern Hemisphere. Dark solid
 400 line and area corresponds to coherent eddies with diameters larger than 120 km, while light gray
 401 dash-dotted line and area shows coherent eddies with diameters smaller than 120 km.

434 6 Regional Climatology

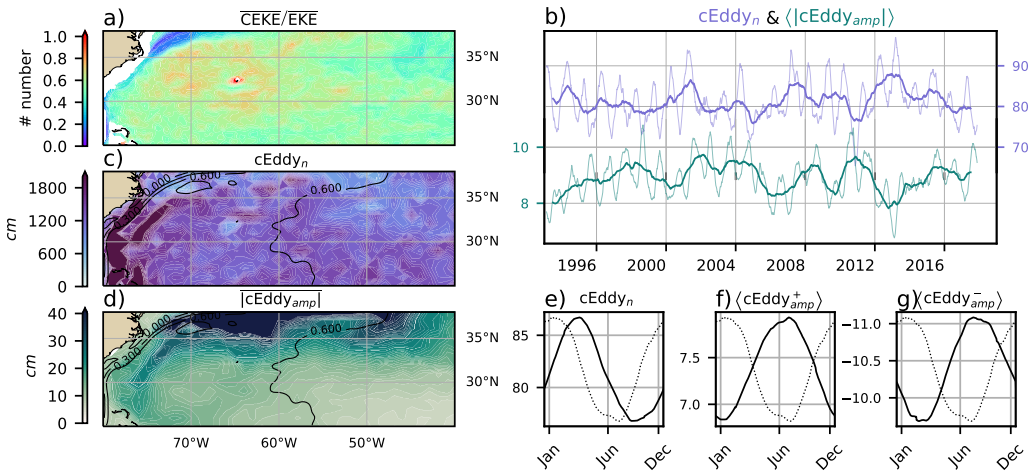
435 For regions with relatively large proportions of CEKE located at boundary extensions
 436 and eastern WBCe and eastern boundary currents, we investigate the seasonal and long-
 437 term variability of the coherent eddy properties.

438 The most energetic western boundary extensions include ; WBCe include the Gulf
 439 Stream, the Kuroshio Current, and the Agulhas Current (Figures 9, 10, and 11). Coher-
 440 ent eddy generation in boundary current extensions occurs through baroclinic and barotropic
 441 instabilities of the mean current, thus all these regions share similar generation dynam-
 442 ics. In all these regions without exception; (i) CEKE contains up to 80% of the EKE
 443 in regions equatorwards equatorward from the mean western boundary extension location WBCe,
 444 (ii) the number of eddies is consistently minimal numbers of eddies small over the mean
 445 western boundary extension WBCe location, and (iii) the eddy amplitude is larger polewards
 446 of the mean western boundary extension over the mean WBCe location.

447 In the Gulf Stream, the energy ratio between CEKE and EKE is ~56% (Figure 9).
 448 The highest energy content ratio occurs in regions with numerous eddies, and collocated



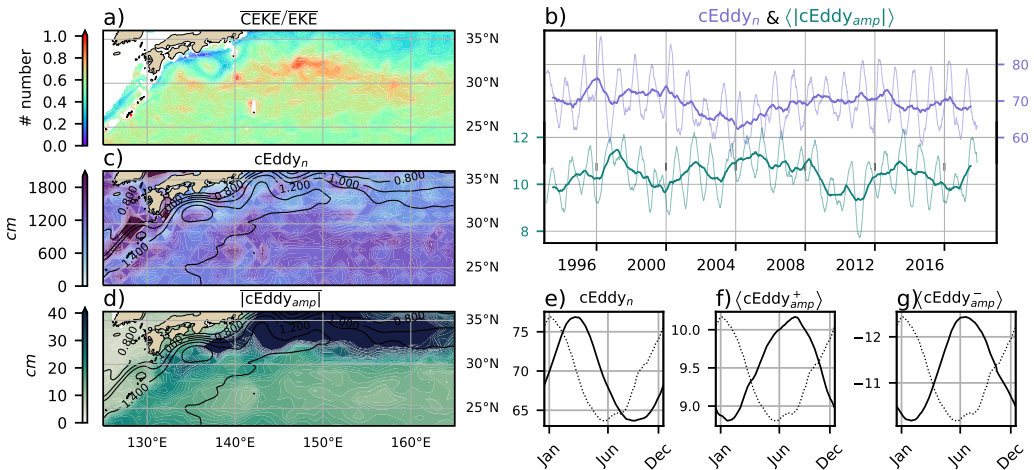
427 **Figure 8.** Trends of coherent eddy statistics. a) and b) Trends of the number of identified
 428 coherent eddies from satellite observations identified using [the TrackEddy scheme of MM19](#), and
 429 those reported in [CheltonCS13](#)'s dataset. c) and d) Trends of the absolute value of identified co-
 430 herent [eddies](#) [eddy](#) amplitude ($cEddy_{[amp]}$) from satellite observations identified using TrackEddy
 431 ([after MM19](#)), and those reported [in Chelton's dataset by CS13](#). e) and f) Trends of [the](#) eddy
 432 amplitude polarity using TrackEddy ($cEddy_{amp}^+$ and $cEddy_{amp}^-$). Gray stippling shows regions
 433 that are statistically significant above the 95% confidence level.



458 **Figure 9.** Climatology of the eddy field and coherent eddy field ~~at-in~~ in the Gulf Stream. a)
 459 Ratio of mean coherent eddy kinetic energy ($\overline{\text{CEKE}}$) versus mean eddy kinetic energy ($\overline{\text{EKE}}$);
 460 b) Thick lines show the running average over 2 years and thin lines show the running average
 461 over 90 days of the coherent eddy number sum and the average coherent eddy amplitude; c)
 462 Map of the number of eddies; d) Map of the average coherent eddy amplitude; e) Seasonal cycle
 463 of the number of eddies (cEddy_n); f) Seasonal cycle of the positive coherent eddy amplitude $\langle |\text{cEddy}_{amp}^+| \rangle$, and g) Seasonal cycle of the negative coherent eddy amplitude $\langle |\text{cEddy}_{amp}^-| \rangle$.
 464 Contours in maps correspond to mean sea surface height (m).

449 with regions where the largest $|\text{cEddy}_{amp}|$ gradients ~~occur~~ occur. The time series of cEddy_n
 450 and $\langle |\text{cEddy}_{amp}| \rangle$ are anti-correlated (-0.52), and they display ~~inter-annual~~ ~~interannual~~
 451 and seasonal variability. Although Chaudhuri et al. (2009) observed ~~that~~ a positive phase
 452 of ~~the~~ North Atlantic Oscillation (NAO) ~~exhibit~~ exhibits higher EKE, due to an increase
 453 in baroclinic ~~instabilities~~ ~~instability~~, thus suggesting more coherent eddies, we do not find
 454 a correlation between the cEddy_n or the $\langle |\text{cEddy}_{amp}| \rangle$ in the Gulf Stream and the NAO
 455 index. Similar to the signal observed in the ~~hemispherical~~ ~~hemispheric~~ analysis, the eddy
 456 count seasonal cycle follows the wind maximum ~~after lagging by~~ \sim 3 months, while the
 457 amplitude of the coherent eddies lags by \sim 6 months.

466 The variability of the cEddy_n and $\langle |\text{cEddy}_{amp}| \rangle$ in the Kuroshio Current are weakly
 467 anti-correlated (-0.41; Figure 10). However, on average 56% of the energy in the region
 468 corresponds to CEKE. As observed in the Gulf Stream, there is an important seasonal
 469 cycle in the boundary ~~extension~~ ~~extension~~, where the eddy count seasonal cycle occurs

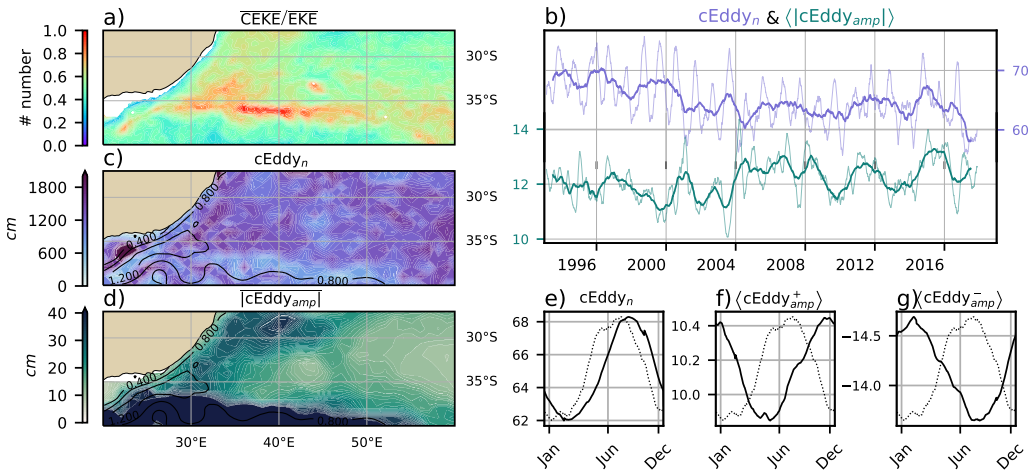


473 **Figure 10.** Climatology of the eddy field and coherent eddy field ~~at-in~~ in the Kuroshio exten-
 474 sion. a) Ratio of mean coherent eddy kinetic energy ($\overline{\text{CEKE}}$) versus mean eddy kinetic energy
 475 ($\overline{\text{EKE}}$); b) Time-series of the coherent eddy number and the average coherent eddy amplitude;
 476 c) Map of the number of eddies; d) Map of the average coherent eddy amplitude; Seasonal cycle
 477 of the e) number of eddies, f) positive coherent eddy amplitude, and g) negative coherent eddy
 478 amplitude. Different lines represent the same as in Figure 9.

470 ~~on March after ~3 months of in March, lagging the wind maximum by ~3 months~~ (January). Meanwhile, the amplitude of the coherent eddies lags ~~the wind maximum~~ by ~
 471 6 months (June) ~~after the maximum wind~~.

479 In the Southern Hemisphere, ~~the~~ the strongest boundary current, the Agulhas Cur-
 480 rent, ~~shows~~ shows similar behavior to its counterparts in the Northern Hemisphere (Figure 11).
 481 On average, coherent eddies in the Agulhas current contain $\sim 56\%$ of the energy, mean-
 482 while the $c\text{Eddy}_n$ seasonal peak occurs in August, while the $\langle |c\text{Eddy}_{amp}| \rangle$ ~~peak~~ occurs
 483 in January–February. The seasonal lag between the winds, eddy count, and eddy ampli-
 484 tude in each of the ~~western boundary current extensions~~ WBCe is interpreted as being
 485 analogous to the ~~explanation observed in Figure 6 of the~~ lagged response of coherent eddy
 486 properties ~~(Figure 6)~~ due to eddy-eddy interactions, consistent with the inverse cascade
 487 of energy.

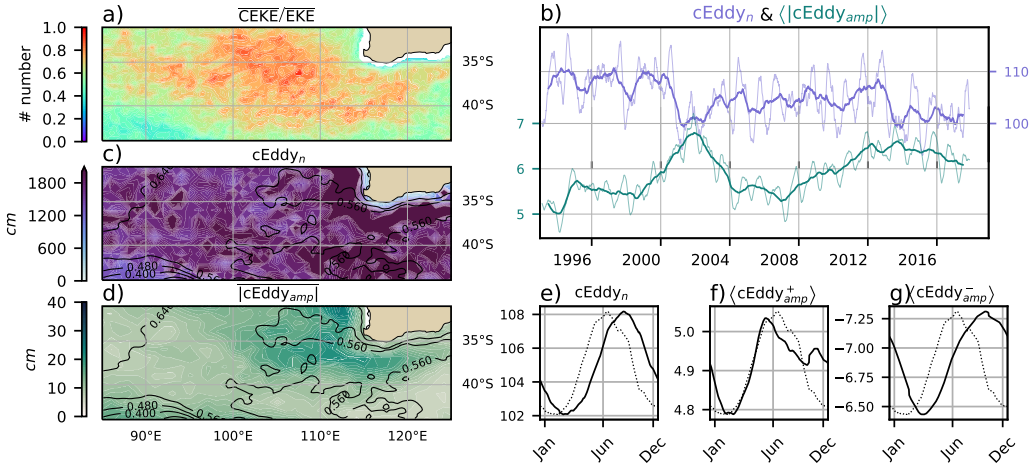
494 Coherent eddies dominate the EKE field in other regions such as the Leeuwin Cur-
 495 rent (Figure 12), where ~~the~~ 65% of the energy is contained by coherent eddies. ~~Although~~



488 **Figure 11.** Climatology of the eddy field and coherent eddy field ~~at-in~~ in the Agulhas Cur-
 489 rent. a) Ratio of mean coherent eddy kinetic energy ($\overline{\text{CEKE}}$) versus mean eddy kinetic energy
 490 ($\overline{\text{EKE}}$); b) Time-series of the coherent eddy number and the average coherent eddy amplitude;
 491 c) Map of the number of eddies; d) Map of the average coherent eddy amplitude; Seasonal cycle
 492 of the e) number of eddies, f) positive coherent eddy amplitude, and g) negative coherent eddy
 493 amplitude. Different lines represent the same as in Figure 9.

496 ~~the-The~~ Leeuwin region is not characterized by having a large EKE, however, a consid-
 497 erable abundance of eddies and large eddy amplitudes are ~~observable~~ observed in the re-
 498 gion. The ~~series-time-series~~ reveal a significant increase in the $\langle |c\text{Eddy}_{amp}| \rangle$, while the
 499 $c\text{Eddy}_n$ has decreased over the last 3 decades ~~(@Andy, you suggested a reference here, I couldn't find it....)~~
 500 The seasonal cycle shows that the $c\text{Eddy}_n$ peak occurs ~~on-in~~ August, 3 months after the
 501 maximum winds (June). Meanwhile, the $\langle c\text{Eddy}_{amp}^+ \rangle$ responds in synchrony to ~~the~~ winds,
 502 and the $\langle c\text{Eddy}_{amp}^- \rangle$ is in phase with the seasonal cycle of the ~~eddy number~~ ($c\text{Eddy}_n$).
 503 Hence, this region contrast the behavior of WBCe, and showcases the spatial variability
 504 of the seasonal cycle of coherent eddies.

511 Another region with important contributions ~~of-to~~ the coherent eddy field is the
 512 East Tropical Pacific (Tehuantepec region; Figure 13), where coherent eddies contain $\sim 58\%$
 513 of the energy. In fact, coherent eddy generation in this region is modulated by winds and
 514 ~~coastally~~ coastally trapped waves which produce a strong horizontal and vertical shear
 515 (baroclinic and barotropic instabilities; Zamudio et al., 2006). Furthermore, the equa-
 516 torial generated waves propagating along the coast have an important interannual vari-

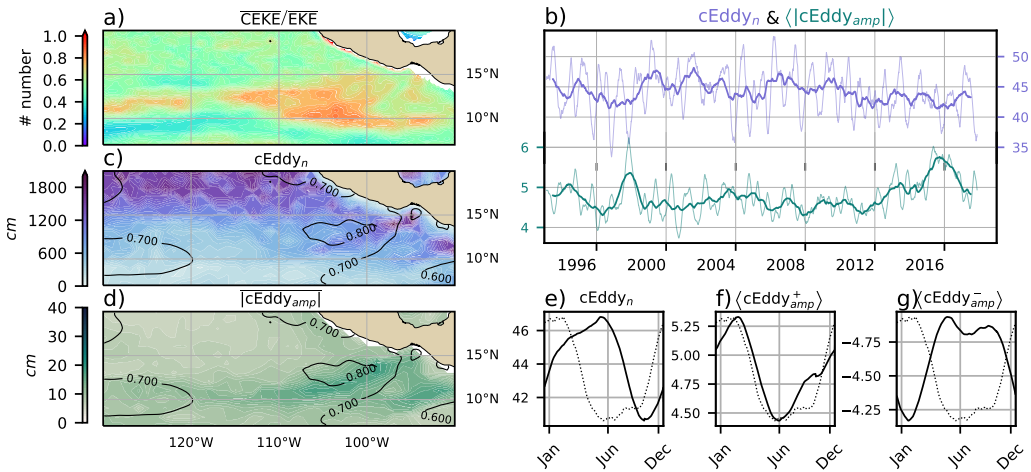


505 **Figure 12.** Climatology of the eddy field and coherent eddy field ~~at-in~~ in the Leeuwin Current
 506 a) Ratio of mean coherent eddy kinetic energy ($\overline{\text{CEKE}}$) versus mean eddy kinetic energy
 507 ($\overline{\text{EKE}}$); b) Time-series of the coherent eddy number and the average coherent eddy amplitude;
 508 c) Map of the number of eddies; d) Map of the average coherent eddy amplitude; Seasonal cycle
 509 of the e) number of eddies; f) positive coherent eddy amplitude, and g) negative coherent eddy
 510 amplitude. Different lines represent the same as in Figure 9.

517 ability observable in the $\langle |c\text{Eddy}_{amp}| \rangle$ time-series, where El Niño events are notable dur-
 518 ing 1997 and 2015 (Figure 13b). The seasonal cycle of $c\text{Eddy}_n$, $\langle c\text{Eddy}_{amp}^+ \rangle$, and $\langle c\text{Eddy}_{amp}^- \rangle$
 519 support the idea of a coherent ~~eddies responding~~ ~~eddy response~~ to two different coher-
 520 ent eddy generation mechanisms; the number of eddies ~~seasonal cycle lags for lags~~ by ~ 3
 521 months from the winds, while the $\langle c\text{Eddy}_{amp}^+ \rangle$ is ~~on-in~~ phase with the winds and the ~~maximum~~
 522 ~~of trapped waves~~ ~~time of maximum trapped wave activity~~ (winter; Zamudio et al., 2006),
 523 ~~and while~~ the $\langle c\text{Eddy}_{amp}^- \rangle$ could be a consequence of eddy-eddy interactions.

530 7 Discussion and Conclusions

531 We ~~have~~ investigated the contribution of coherent eddies ~~in the to the total~~ kinetic
 532 energy field using ~~available~~ satellite observations. We ~~corroborate~~ ~~found~~ that around half
 533 of the EKE is explained by coherent eddies. This half is concentrated in eddy-rich re-
 534 gions where ~~an a recent multi-decadal~~ intensification of the eddy field has been observed
 535 (Martínez-Moreno et al., 2021). The energy contained by eddies is larger than the pre-
 536 vious estimate of 40% by Chelton et al. (2011). Although there are ~~difference~~ ~~differences~~



524 **Figure 13.** Climatology of the eddy field and coherent eddy field ~~at-in~~ in the East Tropical Pa-
 525 cific. a) Ratio of mean coherent eddy kinetic energy ($\overline{\text{CEKE}}$) versus mean eddy kinetic energy
 526 ($\overline{\text{EKE}}$); b) Time-series of the coherent eddy number and the average coherent eddy amplitude;
 527 c) Map of the number of eddies; d) Map of the average coherent eddy amplitude; Seasonal cycle
 528 of the e) number of eddies, f) positive coherent eddy amplitude, and g) negative coherent eddy
 529 amplitude. Different lines represent the same as in Figure 9.

537 in the identification criteria of both eddy identification methods, the main cause of the
 538 difference is ~~believed likely~~ to be the lifespan and amplitude filters. These filters are widely
 539 used to track individual eddies ~~on-in~~ space and time, however, interactions between ed-
 540 dies in energetic regions ~~my may~~ obscure the abundance and influence of short-lived co-
 541 herent eddies. Filters are not used in this study, and indeed a lack of filters could ~~facilitates~~
 542 ~~an under or facilitate an~~ over-estimation of the the energy contained by coherent eddies,
 543 when ~~miss-identifying or miss-fitting~~ mis-identifying or mis-fitting a coherent eddy. ~~Thus,~~
 544 ~~the presented estimate represents an upper limit of the energy contained by coherent eddies.~~

545

546 In addition, it should be noted that regions with first baroclinic Rossby radius of
 547 deformation smaller than 10km cannot be resolved by satellite observations. Thus, the
 548 energy contained by coherent eddies around latitudes of 60° and those near the shore
 549 are missed from this estimate, and ~~remains unknown~~ their role in the seasonal cycle and
 550 local dynamics ~~remains unknown~~. New satellite altimeter missions (e.g. Surface Water

551 and Ocean Topography; SWOT) may allow ~~to estimate~~ estimates of the energy contained
 552 by mesoscale coherent eddies outside the tropical region and the continental slope.

553 ~~Hemispherical Hemisphere-wide~~ variability indicates a strong seasonal cycle of the
 554 EKE, CEKE, and eddy properties. The seasonal cycle of the CEKE in each hemisphere
 555 occurs as a consequence of numerous small coherent eddies interacting with each other
 556 (eddy-eddy interactions) and resulting in stronger, larger and more energetic ~~(but fewer)~~
 557 coherent eddies during summer, after a few months of the yearly coherent eddy number
 558 maxima. This ~~results~~ result reveals eddy-eddy interactions and thus the transfer of en-
 559 ergy from smaller coherent eddies to larger coherent eddies could explain the observed
 560 seasonal cycle of CEKE and coherent eddies properties.

561 Coherent eddy properties ~~showcase~~ reveal a non-uniform long-term readjustment
 562 of the mesoscale eddy field. Overall, the eddy number has decreased globally at a sig-
 563 nificant rate of ~ 35 eddies per decade from ~ 4000 eddies identified globally on average
 564 each day. However, large proportions of the ocean show ~~an-a~~ strengthening of the mesoscale
 565 coherent eddy field at a rate greater than ~ 1 cm per decade. This strengthening of the
 566 coherent eddy amplitude is attributed to an intensification of each coherent eddy polar-
 567 ity, rather than a readjustment of the coherent eddy field to sea level rise. In other words,
 568 the coherent eddy amplitude intensification is occurring in both coherent eddy polar-
 569 ities and ~~explain~~ explains a proportion of the previously observed readjustments in the
 570 eddy field to long-term changes in the ocean forcing (Hu et al., 2020; Wunsch, 2020; Martínez-
 571 Moreno et al., 2021). This long-term readjustment ~~showcases~~ reveals an intensification
 572 of the coherent eddy field, possibly due to long-term readjustments in the ocean baro-
 573 clinic and barotropic instabilities, as well as the strength of the winds.

574 The reconstruction of the coherent eddies and their statistics ~~have~~ has revealed re-
 575 gions with important coherent eddy contributions and a distinct seasonal evolution of
 576 the coherent eddies. ~~Remarkably, western boundary extensions~~ Western boundary current
 577 extensions (WBCe) generate eddies through the instability of the main currents and the
 578 seasonal cycle of coherent eddies, CEKE, and thus EKE could be associated with an in-
 579 verse energy cascade observable through lagged seasonal cycles in the coherent eddy statis-
 580 tics. In addition ~~to this~~, the amplitude of the seasonal cycle in ~~the boundary extensions~~
 581 WBCe is two times larger than any other region, thus the seasonality of the coherent ed-
 582 dies in ~~boundary extensions dominate the hemispherical~~ WBCe dominates the hemispheric

583 seasonal cycle. Furthermore, the seasonal lag of the inverse energy cascade is coupled
 584 with the presence of fronts (Qiu et al., 2014), such is the case ~~of western boundary extensions for~~
 585 ~~WBCe~~, and our results are consistent with the notion of baroclinic instability generat-
 586 ing eddies and ~~through~~ ~~via~~ eddy-eddy interactions ~~an~~ ~~a~~ lagged inverse energy cascade.

587 The use of satellite observations in this study ~~limit~~ ~~limits~~ our ability to quantify
 588 the importance of the inverse energy cascade seasonality in the control of the coherent
 589 eddy seasonal cycle. As mentioned above, there is robust evidence of an increase in eddy-
 590 eddy interactions, however we ~~can not~~ ~~cannot~~ discard important contributions from other
 591 processes such as the seasonal cycle of forcing, ~~stratification~~, and instabilities, which are
 592 crucial in the generation of coherent eddies. Although this study can provide a descrip-
 593 tive response of the coherent eddy field, further ~~studies~~ ~~work is~~ are needed to asses the
 594 role of eddy-eddy interactions in our changing climate, ocean dynamics, and biogeochem-
 595 ical process. Furthermore, the SWOT mission could allow ~~us~~ to advance our understand-
 596 ing of eddy-eddy interactions and the seasonal cycle of scales smaller than mesoscale, which
 597 may provide further evidence of the inverse energy cascade driving the coherent eddy
 598 seasonality.

599 Acknowledgments

600 Chelton & Schlax (2013) dataset was produced by SSALTO/DUACS and distributed by
 601 AVISO+ (<https://www.aviso.altimetry.fr/>) with support from CNES, developed
 602 and validated in collaboration with E.Mason at IMEDEA. Global coherent eddy recon-
 603 struction, coherent and ~~non-coherent~~ ~~non-coherent~~ eddy kinetic energy datasets, in ad-
 604 dition to gridded coherent eddy tracking datasets are publicly available at (<https://doi.org/10.5281/zenodo.4646429>). All analyses and figures in this manuscript are re-
 605 producible via Jupyter notebooks and instructions can be found in the Github repos-
 606 itory CEKE_climatology (https://github.com/josuemtzmo/CEKE_climatology). Trends
 607 used the Python Package xarrayMannKendall (<https://doi.org/10.5281/zenodo.4458776>).
 608 ~~J.M.-M. was supported by the Consejo Nacional de Ciencia y Tecnología (CONACYT),~~
 609 ~~Mexico funding. M.H.E. is supported by the Centre for Southern Hemisphere Oceans~~
 610 ~~Research (CSHOR), a joint research centre between Qingdao National Laboratory for~~
 611 ~~Marine Science and Technology (QNL), Commonwealth Scientific and Industrial Research~~
 612 ~~Organisation (CSIRO), University of New South Wales (UNSW), and the University of~~
 613 ~~Tasmania (UTAS). Analyses were undertaken on the National Computational Infrastructure~~

615 [in Canberra, Australia, which is supported by the Australian Commonwealth Government.](#)

616

617 **References**

- 618 Arbic, B. K., Polzin, K. L., Scott, R. B., Richman, J. G., & Shriver, J. F. (2013).
 619 On Eddy Viscosity, Energy Cascades, and the Horizontal Resolution of Gridded
 620 Satellite Altimeter Products*. *Journal of Physical Oceanography*, 43(2), 283–300.
 621 doi: 10.1175/jpo-d-11-0240.1
- 622 Ashkezari, M. D., Hill, C. N., Follett, C. N., Forget, G., & Follows, M. J. (2016).
 623 Oceanic eddy detection and lifetime forecast using machine learning methods.
 624 *Geophysical Research Letters*, 43(23). doi: 10.1002/2016gl071269
- 625 Beron-Vera, F. J., Wang, Y., Olascoaga, M. J., Goni, G. J., & Haller, G. (2013). Objective
 626 Detection of Oceanic Eddies and the Agulhas Leakage. *Journal of Physical
 627 Oceanography*, 43(7), 1426–1438. doi: 10.1175/JPO-D-12-0171.1
- 628 Bouali, M., Sato, O. T., & Polito, P. S. (2017). Temporal trends in sea surface tem-
 629 perature gradients in the South Atlantic Ocean. *Remote Sensing of Environment*,
 630 194, 100–114. doi: 10.1016/j.rse.2017.03.008
- 631 Callies, J., Flierl, G., Ferrari, R., & Fox-Kemper, B. (2015). The role of mixed-layer
 632 instabilities in submesoscale turbulence. *Journal of Fluid Mechanics*, 788, 5–41.
 633 doi: 10.1017/jfm.2015.700
- 634 Cane, M. A., Clement, A. C., Kaplan, A., Kushnir, Y., Pozdnyakov, D., Seager, R.,
 635 ... Murtugudde, R. (1997). Twentieth-Century Sea Surface Temperature Trends.
 636 *Science*, 275(5302), 957–960. doi: 10.1126/science.275.5302.957
- 637 Chaudhuri, A. H., Gangopadhyay, A., & Bisagni, J. J. (2009). Interannual variabil-
 638 ity of Gulf Stream warm-core rings in response to the North Atlantic Oscillation.
 639 *Continental Shelf Research*, 29(7), 856–869. doi: 10.1016/j.csr.2009.01.008
- 640 Chelton, D. B., A. d. R., Schlax, M. G., Naggar, K., & Siwertz, N. (1998). Geo-
 641 graphical variability of the first baroclinic Rossby radius of deformation. *Journal
 642 of Physical Oceanography*, 28(3), 433–460. doi: 10.1175/1520-0485(1998)028<433:
 643 GVOTFB>2.0.CO;2
- 644 Chelton, D. B., Gaube, P., Schlax, M. G., Early, J. J., & Samelson, R. M. (2011).
 645 The influence of nonlinear mesoscale eddies on near-surface oceanic chlorophyll.
 646 *Science*, 334(6054), 328–32. doi: 10.1126/science.1208897

- 647 Chelton, D. B., & Schlax, M. G. (2013). *Mesoscale eddies in altimeter observations*
648 *of ssh.*
- 649 Chelton, D. B., Schlax, M. G., Samelson, R. M., & de Szoeke, R. A. (2007). Global
650 observations of large oceanic eddies. *Geophysical Research Letters*, 34(15),
651 L15606. doi: 10.1029/2007GL030812
- 652 CMEMS. (2017). The Ssalto/Duacs altimeter products were produced and dis-
653 tributed by the Copernicus Marine and Environment Monitoring Service. *Aviso*
654 *Dataset.* Retrieved from <https://www.aviso.altimetry.fr/>
- 655 Cui, W., Wang, W., Zhang, J., & Yang, J. (2020). Identification and census statis-
656 tics of multicore eddies based on sea surface height data in global oceans. *Acta*
657 *Oceanologica Sinica*, 39(1), 41–51. doi: 10.1007/s13131-019-1519-y
- 658 Faghmous, J. H., Frenger, I., Yao, Y., Warmka, R., Lindell, A., & Kumar, V. (2015,
659 6). A daily global mesoscale ocean eddy dataset from satellite altimetry. *Scientific*
660 *Data*, 2, 150028 EP -. doi: 10.1038/sdata.2015.28
- 661 Ferrari, R., & Wunsch, C. (2009). Ocean Circulation Kinetic Energy: Reservoirs,
662 Sources, and Sinks. *Annual Review of Fluid Mechanics*, 41(1), 253–282. doi: 10
663 .1146/annurev.fluid.40.111406.102139
- 664 Frenger, I., Gruber, N., Knutti, R., & Münnich, M. (2013). Imprint of Southern
665 Ocean eddies on winds, clouds and rainfall. *Nature Geoscience*, 6(8), 608 EP -.
666 doi: 10.1038/ngeo1863
- 667 Frenger, I., Münnich, M., Gruber, N., & Knutti, R. (2015). Southern Ocean eddy
668 phenomenology. *Journal of Geophysical Research: Oceans*, 120(11), 7413-7449.
669 doi: 10.1002/2015JC011047
- 670 Fu, L., Chelton, D., Le Traon, P., & Oceanography, M. R. (2010). Eddy dynamics
671 from satellite altimetry. *Oceanography*, 23(4), 14-25. doi: 10.2307/24860859
- 672 Gill, A., Green, J., & Simmons, A. (1974). Energy partition in the large-scale ocean
673 circulation and the production of mid-ocean eddies. *Deep Sea Res Oceanogr Abstr*,
674 21(7), 499-528. doi: 10.1016/0011-7471(74)90010-2
- 675 Hogg, A. M., & Blundell, J. R. (2006). Interdecadal variability of the southern
676 ocean. *Journal of Physical Oceanography*, 36(8), 1626-1645. doi: 10.1175/
677 JPO2934.1
- 678 Hogg, A. M., Meredith, M. P., Chambers, D. P., Abrahamsen, E. P., Hughes,
679 C. W., & Morrison, A. K. (2015). Recent trends in the Southern Ocean

- 680 eddy field. *Journal of Geophysical Research: Oceans*, 120(1), 257-267. doi:
681 10.1002/2014JC010470
- 682 Hu, S., Sprintall, J., Guan, C., McPhaden, M. J., Wang, F., Hu, D., & Cai,
683 W. (2020, 2). Deep-reaching acceleration of global mean ocean circula-
684 tion over the past two decades. *Science Advances*, 6(6), eaax7727. doi:
685 10.1126/sciadv.aax7727
- 686 Japan Meteorological Agency, Japan. (2013). *Jra-55: Japanese 55-year reanalysis,*
687 *daily 3-hourly and 6-hourly data.* Boulder CO: Research Data Archive at the Na-
688 tional Center for Atmospheric Research, Computational and Information Systems
689 Laboratory. Retrieved from <https://doi.org/10.5065/D6HH6H41>
- 690 Kang, D., & Curchitser, E. N. (2013). Gulf stream eddy characteristics in a high-
691 resolution ocean model. *Journal of Geophysical Research: Oceans*, 118(9), 4474-
692 4487. Retrieved from <https://agupubs.onlinelibrary.wiley.com/doi/abs/10.1002/jgrc.20318> doi: <https://doi.org/10.1002/jgrc.20318>
- 693 Kang, D., & Curchitser, E. N. (2017). On the Evaluation of Seasonal Variability of
694 the Ocean Kinetic Energy. *Geophysical Research Letters*, 47, 1675-1583. doi: 10
695 .1175/JPO-D-17-0063.1
- 696 Li, G., Cheng, L., Zhu, J., Trenberth, K. E., Mann, M. E., & Abraham, J. P. (2020).
697 Increasing ocean stratification over the past half-century. *Nature Climate Change*,
698 1–8. doi: 10.1038/s41558-020-00918-2
- 699 Martínez-Moreno, J., Hogg, A. M., England, M., Constantinou, N. C., Kiss, A. E.,
700 & Morrison, A. K. (2021). Global changes in oceanic mesoscale currents over the
701 satellite altimetry record. *Journal of Advances in Modeling Earth Systems*, 0(ja).
702 doi: 10.1029/2019MS001769
- 703 Martínez-Moreno, J., Hogg, A. M., Kiss, A. E., Constantinou, N. C., & Morrison,
704 A. K. (2019). Kinetic energy of eddy-like features from sea surface altime-
705 try. *Journal of Advances in Modeling Earth Systems*, 11(10), 3090-3105. doi:
706 10.1029/2019MS001769
- 707 Patel, R. S., Llort, J., Strutton, P. G., Phillips, H. E., Moreau, S., Pardo, P. C.,
708 & Lenton, A. (2020). The Biogeochemical Structure of Southern Ocean
709 Mesoscale Eddies. *Journal of Geophysical Research: Oceans*, 125(8). doi:
710 10.1029/2020jc016115
- 711 Pilo, G. S., Mata, M. M., & Azevedo, J. L. L. (2015). Eddy surface properties and

- 713 propagation at Southern Hemisphere western boundary current systems. *Ocean*
714 *Science*, 11(4), 629–641. doi: 10.5194/os-11-629-2015
- 715 Qiu, B. (1999). Seasonal Eddy Field Modulation of the North Pacific Subtropical
716 Countercurrent: TOPEX/Poseidon Observations and Theory. *Journal of Physical*
717 *Oceanography*, 29(10), 2471–2486. doi: 10.1175/1520-0485(1999)029<2471:sefmot>2
718 .0.co;2
- 719 Qiu, B., & Chen, S. (2004). Seasonal Modulations in the Eddy Field of the South
720 Pacific Ocean. *Journal of Physical Oceanography*, 34(7), 1515–1527. doi: 10.1175/
721 1520-0485(2004)034<1515:smitef>2.0.co;2
- 722 Qiu, B., Chen, S., Klein, P., Sasaki, H., & Sasai, Y. (2014). Seasonal Mesoscale
723 and Submesoscale Eddy Variability along the North Pacific Subtropical Coun-
724 tercurrent. *Journal of Physical Oceanography*, 44(12), 3079–3098. doi:
725 10.1175/JPO-D-14-0071.1
- 726 Ruela, R., Sousa, M. C., deCastro, M., & Dias, J. M. (2020). Global and regional
727 evolution of sea surface temperature under climate change. *Global and Planetary*
728 *Change*, 190, 103190. doi: 10.1016/j.gloplacha.2020.103190
- 729 Sasaki, H., Klein, P., Qiu, B., & Sasai, Y. (2014). Impact of oceanic-scale inter-
730 actions on the seasonal modulation of ocean dynamics by the atmosphere. *Nature*
731 *Communications*, 5(1), 5636. doi: 10.1038/ncomms6636
- 732 Schubert, R., Schwarzkopf, F. U., Baschek, B., & Biastoch, A. (2019). Submesoscale
733 Impacts on Mesoscale Agulhas Dynamics. *Journal of Advances in Modeling Earth*
734 *Systems*, 11(8), 2745–2767. doi: 10.1029/2019ms001724
- 735 Siegel, D., Peterson, P., DJ, M., Maritorena, S., & Nelson, N. (2011). Bio-optical
736 footprints created by mesoscale eddies in the Sargasso Sea. *Geophysical Research*
737 *Letters*, 38(13), n/a-n/a. doi: 10.1029/2011GL047660
- 738 Uchida, T., Abernathey, R., & Smith, S. (2017). Seasonality of eddy kinetic energy
739 in an eddy permitting global climate model. *Ocean Modelling*, 118, 41–58. doi: 10
740 .1016/j.ocemod.2017.08.006
- 741 Wunsch, C. (2020). Is The Ocean Speeding Up? Ocean Surface Energy Trends.
742 *Journal of Physical Oceanography*, 50(11), 1–45. doi: 10.1175/jpo-d-20-0082.1
- 743 Wunsch, C., & Ferrari, R. (2004). Vertical mixing, energy, and the general circula-
744 tion of the oceans. *Annual Review of Fluid Mechanics*, 36(1), 281–314. doi: 10
745 .1146/annurev.fluid.36.050802.122121

- 746 Wyrtki, K., Magaard, L., & Hager, J. (1976). Eddy energy in the oceans. *Journal of*
747 *Geophysical Research*, 81(15), 2641-2646. doi: 10.1029/JC081i015p02641
- 748 Yue, S., & Wang, C. (2004). The Mann-Kendall Test Modified by Effective Sample
749 Size to Detect Trend in Serially Correlated Hydrological Series. *Water Resources*
750 *Management*, 18(3), 201–218. doi: 10.1023/b:warm.0000043140.61082.60
- 751 Zamudio, L., Hurlbert, H. E., Metzger, E. J., Morey, S. L., O'Brien, J. J., Tilburg,
752 C., & Zavala-Hidalgo, J. (2006). Interannual variability of Tehuantepec ed-
753 dies. *Journal of Geophysical Research: Oceans (1978–2012)*, 111(C5). doi:
754 10.1029/2005JC003182